The Pennsylvania State University

The Graduate School

ON THE USE OF THE THIN-BOUNDARY-LAYER EQUATIONS IN NUMERICAL SIMULATIONS OF SUPERCELL STORMS

A Thesis in

Meteorology and Atmospheric Science

by

Kiley Q. Allen

Submitted in Partial Fulfillment

of the Requirements

for the Degree of

Master of Science

August 2024

The thesis of Kiley Q. Allen was reviewed and approved by the following:

Paul Markowski
Distinguished Professor of Meteorology and Department Head
Thesis Co-Advisor

Ying Pan
Associate Professor of Meteorology and Atmospheric Science
Thesis Co-Advisor

Yvette Richardson
Professor of Meteorology and Senior Associate Dean of Undergraduate Education, College of Earth and Mineral Sciences
Committee Member

Abstract

Three relatively high resolution (75-m horizontal grid spacing), large eddy simulation (LES) ensembles of tornadic supercell storms, varying only in their parameterization of near-surface turbulence, were created in order to investigate the effect of a more realistic treatment of the lower boundary condition on supercell storm simulations. One ensemble uses the semislip scheme, while the other two employ versions of the "thin-boundary-layer equations" (TBLE) approach. Small, random temperature perturbations introduced via initial conditions lead to quasi-steady-state, turbulent boundary layers after 12 h of spinup. Subsequently, the supercell storms are initiated via a warm bubble. Each storm becomes a long-lived supercell with an intense mesocyclone and at least one tornado-like vortex (TLV). The use of the TBLE approach causes surface-layer turbulent coherent structures to be stronger and more numerous in both the pre-storm and near-storm environments. Additionally, notable differences in reflectivity, TLV intensity, and TLV duration are found. These differences are ultimately attributable to the ensembles' near-surface turbulence parameterization. The severe storms community should strive to gain a better understanding of the limitations posed by different lower boundary conditions and near-surface turbulence parameterizations, as well as storm simulations' sensitivity to such constraints.

Table of Contents

List of Figures

List of Tables

Acknowledgments

I would like to offer my thanks to my advisors Paul Markowski and Ying Pan for their support on this project and of me throughout my time in graduate-level academia. I would also like to thank Yvette Richardson for taking the time to serve on my master's committee and for her helpful insight on this work. Finally, I would like to thank my parents, Brent and Leith Allen, and my significant other, William Kortright, as their unwavering support and confidence in me has made this work possible.

This research was supported by NSF Award 2150792. The findings and conclusions of this work solely represent the views of the author and do not necessarily represent the views of the National Science Foundation. Computations for this research were performed on the National Center for Atmospheric Research's (NCAR) Cheyenne and Derecho supercomputers.

Chapter 1

Introduction

Convective storm modeling has greatly improved our understanding of supercell dynamics and tornadogenesis, especially because observations in storms are challenging to obtain. Klemp and Wilhelmson's (1978) approach to the three-dimensional simulation of convective storms has long been the industry standard. A substantial portion of our current understanding of supercells stems from the pioneering studies following shortly thereafter in the late 1970s–1980s. These studies' simulations were idealized, using various simplifying assumptions and parameterizations (e.g., no Coriolis acceleration, no heat or moisture surface fluxes, and warm-rain microphysics). Deardorff's (1980) large eddy simulation (LES; Moeng and Sullivan 1994) closure was used in these early storm simulations, although it was acknowledged that model resolution was too coarse to resolve the large, energy-containing eddies (a requirement of LES closure).

From these early storm simulations, it has been accepted that supercell updrafts develop their characteristic rotation[1] by reorienting the horizontal vortex lines existing within a vertically sheared environment into the vertical (Rotunno 1981; Rotunno and Klemp 1985).

[1]Supercell storms occur in environments with large vertical wind shear, and, by definition, contain persistent "mesocyclones" (deep regions of vertical vorticity (ζ) with a characteristic width of 3–8 km and a magnitude of O(10^{-2}) s^{-1}; Markowski and Richardson 2010).

These studies also revealed that supercells, unlike ordinary thunderstorms, have significant dynamic pressure perturbations that lead to their tendency to propagate to the right of the mean environmental wind direction. Supercells' rightward storm motion leads to low-altitude storm-relative winds that tend to have a significant component aligned with the horizontal vorticity ($\boldsymbol{\omega}_h$) present in the environment. This "streamwise" orientation of the supercell with respect to the environmental vortex lines facilitates $\boldsymbol{\omega}_h$ tilting and the storm's establishment of net cyclonic rotation (Rotunno and Klemp 1982; Davies-Jones 1984; Rotunno and Klemp 1985). Early simulations also indicated that the vertical vorticity (ζ) necessary for tornadogenesis, which must exist at the surface, could pre-exist within the environment, or be provided by storm baroclinicity and downdrafts (Davies-Jones 1982a,b; Davies-Jones and Brooks 1993).

Until the mid-1990s, the "free slip" lower boundary condition was predominantly used in convective storm simulations. The traditional definition of the free slip lower boundary condition (commonly used in the engineering community) takes shear stress to be zero at the surface; however, this implies a non-zero vertical gradient of shear stress at the model's lowest grid level for horizontal winds (on a C grid, this would be $z = 0.5\Delta z$). To mitigate this, Klemp and Wilhelmson (1978) used a modified version of the free slip lower boundary condition that takes the vertical gradient of shear stress to be zero at the model's lowest grid level for horizontal winds. Physically, this implies that the vertical gradient of subgrid-scale (SGS) shear stress does not contribute to the evolution of the resolved horizontal velocity field at the model's lowest grid level. Klemp and Wilhelmson's (1978) free slip lower boundary condition was frequently employed in storm simulations because of its ability to maintain a steady environmental wind profile.

In the mid-1990s, the Wicker and Wilhelmson (1995) supercell simulation exploring tornadogenesis and tornado decay employed the so-called "semislip" scheme, rather than

the free slip lower boundary condition. The semislip scheme defines the stress at the lower boundary in terms of the wind speed at the first horizontal grid level squared, multiplied by a roughness-length-dependent drag coefficient. This alternative treatment of the lower boundary condition assumes that stress is locally and instantaneously related to the squared velocity just above the ground. This idealization is questionable under the unsteady and horizontally heterogeneous conditions prevalent in storms and near-storm environments.

The "thin-boundary-layer equations" (TBLE) approach has been used by the engineering community to get around some of the limitations imposed by the semislip scheme (Balaras et al. 1996; Cabot 1996). Wang et al. (2023) recently implemented the TBLE approach into Cloud Model 1 (CM1; Bryan and Fritsch 2002), and demonstrated that it effectively "breaks" the semislip scheme's assumption of a locally instantaneous equilibrium between surface stress and near-surface horizontal velocity. The semislip scheme and TBLE approach both will be discussed in more detail in Chapter 2.

Additionally, as computational capabilities increase, supercell simulations also have improved in resolution and boundary layer character. Until recently, supercells have been simulated in laminar environments, ignoring the turbulent nature of the atmospheric boundary layer (ABL). Beginning with Nowotarski et al. (2014), modern supercell simulations have started making efforts to include fully turbulent environments. Most modern supercell simulations are also now using LES-appropriate horizontal grid spacing—and, in some cases, are able to resolve tornado-like vortices [TLVs; this term is preferred over "tornado" when simulations use grid spacings larger than $\sim$25 m (horizontal) and $\sim$10 m (vertical), since such grids are not able to resolve some tornado-specific flow features; Markowski (2020)].

Markowski (2020) recently developed a high-resolution (75-m horizontal grid spacing) 25-member ensemble of supercell storm simulations using a fully turbulent environment to study the intrinsic predictability of tornadic supercells. Subsequently, Markowski (2024) re-

examined one of these tornadic supercell simulations, and found that its simulated TLV had been primarily fueled by environmental air parcels and ambient vorticity during tornadogenesis. This result stands in contrast to the aforementioned findings of the late 20th century, that downdrafts and baroclinic outflow are key for tornadogenesis. Markowski (2024) also uncovered a new potential pathway for tornadogenesis that hinges on resolved turbulent coherent structures, or eddies, in the surface layer (Fig. 1.1).

As seen in the Markowski (2020, 2024) simulations, the shear-dominated atmospheric surface layer [ASL; the lowest $\sim$100 m above ground level (AGL)] is characterized by horizontal velocity streaks aligned with the ground-relative mean wind direction. These streaks alternate in their velocity strength, with air sinking (rising) where velocity is faster (slower). These horizontal gradients in horizontal velocity imply streaks of ζ, which have been connected to the presence of the aforementioned coherent structures in the turbulent boundary layer (Alfonsi 2006; Davidson 2015; Markowski 2024). Markowski (2024) describes how these turbulent coherent structures cause vertical corrugations in the environmental vortex lines, which can be further tilted and stretched into a TLV when the storm updraft passes over them. Given the potential importance of surface layer turbulent coherent structures, it is reasonable to expect that altering a storm simulation's near-surface turbulence parameterization might influence these coherent structures.

This thesis uses modified Markowski (2020) high-resolution supercell simulations to explore how the use of a more justifiable lower boundary condition affects surface-layer turbulent coherent structures, TLVs, and supercells. Three ensembles of supercell simulations, varying only in near-surface turbulence parameterization, are performed: one ensemble uses the semislip scheme, and the other two use the Balaras TBLE and Cabot TBLE schemes. Chapter 2 describes each of these near-surface turbulence parameterizations and simulation ensembles in greater detail.

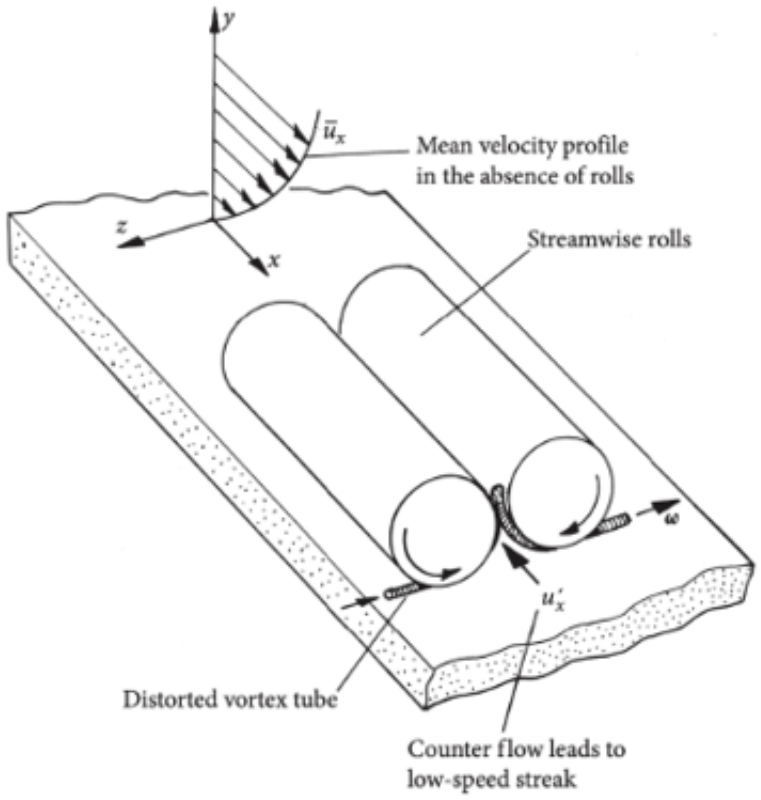

Figure 1.1. A pair of ASL counter-rotating coherent structures and their interaction with an environmental vortex line, as illustrated by Davidson (2015, p. 136).

Chapter 2

Methodology

2.1 Numerical Simulation Configuration

The simulations in this study are performed using CM1 (Bryan and Fritsch 2002) and are configured following Markowski (2020), except for a few modifications. The first major modification is the use of the TBLE as a surface-layer parameterization in addition to the semislip scheme (see subsection 2.2 for more details). Because the TBLE approach was implemented into CM1 release 19.6 (Wang et al. 2023), this study uses release 19.6 instead of release 18.3 (the version of CM1 used by Markowski 2020). As the second major modification, the weighted essentially non-oscillatory (WENO) scheme is turned off for momentum advection, in order to avoid unrealistic suppression of turbulent motions in LES (Wang et al. 2021). The WENO scheme for scalar advection remains on, as it is critical for avoiding spurious oscillations near sharp scalar gradients, such as cloud edges in storm simulations (Shu 2003). Additionally, the number of grid points in the domain has slightly increased from $1700 \times 1700 \times 121$ to $1728 \times 1728 \times 121$, because the supercomputer used to run these simulations has a different number of processors per node than the supercomputer used in Markowski (2020). The grid spacing remains unchanged, with 75-m horizontal grid

spacing and vertical grid spacing varying from 15 m at the surface to 285 m at the top of the domain. Consequently, the domain size is slightly larger than Markowski's (2020), having increased from 127.5 km × 127.5 km × 18.0 km to 129.6 km × 129.6 km × 18.0 km.

All other configurations are identical to those in Markowski (2020). As a brief summary, the lateral boundaries are periodic, the top boundary is rigid and free-slip, and the bottom boundary is a flat surface characterized by a roughness length of $z_0 = 0.12$ m with zero heat and moisture flux. The National Severe Storms Laboratory (NSSL) double-moment microphysics scheme is employed. The Coriolis acceleration only acts on horizontal velocity perturbations relative to the initial base state, and radiative transfer is excluded.

2.2 Near-Surface Turbulence Parameterizations

Three five-member storm simulation ensembles were performed in order to explore the effect of using a more realistic lower boundary treatment in supercell simulations. Each ensemble uses a different near-surface turbulence parameterization: one uses the aforementioned semislip scheme, and the other two use the Balaras and Cabot TBLE approaches, respectively.

The semislip scheme defines the stress at the model's lower boundary in terms of the square of the wind speed at the model's first horizontal grid level, multiplied by a non-dimensional drag coefficient that depends on roughness length:

$$\boldsymbol{\tau}_w = -c_d \widetilde{\mathbf{U}}_\mathbf{1} \widetilde{U}_1 \tag{2.1}$$

Here, $\boldsymbol{\tau}_w$ denotes the stress at the lower boundary, or "at the wall," and is defined as the vector combination of the τ_{13} and τ_{23} components of the subgrid-scale (SGS) stress tensor, $\boldsymbol{\tau}_{ij}$. The non-dimensional drag coefficient is given by c_d, $\widetilde{\mathbf{U}}_\mathbf{1}$ is the ground-relative horizontal

velocity at the model's first horizontal grid level, and $\widetilde{U}_1$ is the magnitude of $\widetilde{\mathbf{U}}_\mathbf{1}$. The semislip scheme is consistent with Monin-Obukhov similarity theory (MOST; Monin and Obukhov 1954),

$$\frac{\partial \widetilde{U}_1}{\partial z} = \frac{u_*}{\kappa z_1}\phi_m, \tag{2.2}$$

where $u_* = |\boldsymbol{\tau}_w|^{1/2}$ is the friction velocity, κ is the von Kármán constant (≈ 0.4), ϕ_m is dimensionless shear, and a tilde represents spatial filtering for LES. MOST inherently assumes an instantaneous, local equilibrium between $\widetilde{\mathbf{U}}_\mathbf{1}$ and $\boldsymbol{\tau}_w$; in other words, the semislip scheme forces the stress at the lower boundary to be proportional to the square of the near-surface wind speed *at every instant and at every grid point*. This assumption is highly unrealistic, because near-surface fluid experiences the effects of surface friction via turbulent eddies, which have finite time and length scales. Therefore, it cannot be assumed that surface effects would be instantaneously or locally communicated to the overlying flow. This assumption is especially problematic near storms where conditions are highly unsteady and horizontally heterogeneous.

The TBLE model, first developed by Balaras et al. (1996) and later adapted by Cabot (1996), is a non-equilibrium approach to the lower boundary condition that includes solving a simplified version of Reynolds-averaged Navier-Stokes (RANS) equations on a second grid set embedded between the LES's bottom boundary and the first grid level (Fig. 2.1). The horizontal grid spacing within this added layer is the same as that of the LES, while the vertical grid spacing is much smaller. The TBLE implemented into CM1 by Wang et al. (2023) are given by:

$$\begin{aligned}
\frac{\partial \overline{u}}{\partial t} + \frac{\partial}{\partial x}\left(\overline{uu}\right) + \frac{\partial}{\partial y}\left(\overline{vu}\right) + \frac{\partial}{\partial z}\left(\overline{wu}\right) &= -\frac{1}{\rho_0}\frac{\partial \overline{p}_{sfc}}{\partial x} + f\overline{v} - \frac{\partial \overline{u'w'}}{\partial z}, \\
\frac{\partial \overline{v}}{\partial t} + \frac{\partial}{\partial x}\left(\overline{uv}\right) + \frac{\partial}{\partial y}\left(\overline{vv}\right) + \frac{\partial}{\partial z}\left(\overline{wv}\right) &= -\frac{1}{\rho_0}\frac{\partial \overline{p}_{sfc}}{\partial y} + f\overline{u} - \frac{\partial \overline{v'w'}}{\partial z},
\end{aligned} \tag{2.3}$$

$$\frac{\partial \overline{u}}{\partial x} + \frac{\partial \overline{v}}{\partial y} + \frac{\partial \overline{w}}{\partial z} = 0.$$

The turbulent fluxes are calculated using eddy-viscosity models,

$$\begin{aligned} -\overline{u'w'} &= \nu_t \left(\frac{\partial \overline{u}}{\partial z} + \frac{\partial \overline{w}}{\partial x} \right) \approx \nu_t \frac{\partial \overline{u}}{\partial z}, \\ -\overline{v'w'} &= \nu_t \left(\frac{\partial \overline{v}}{\partial z} + \frac{\partial \overline{w}}{\partial y} \right) \approx \nu_t \frac{\partial \overline{v}}{\partial z}, \end{aligned} \tag{2.4}$$

where ν_t is the eddy viscosity with a dimension of length multiplied by velocity. The Balaras TBLE model (Balaras et al. 1996) uses the eddy viscosity model

$$\nu_t = [\kappa (z + z_0)]^2 |\overline{S}|, \tag{2.5}$$

where z_0 is roughness length, and $|\overline{S}|$ is the magnitude of the mean strain-rate tensor and can be approximated as

$$|\overline{S}| \approx \left[\left(\frac{\partial \overline{u}}{\partial z} \right)^2 + \left(\frac{\partial \overline{v}}{\partial z} \right)^2 \right]^{\frac{1}{2}}. \tag{2.6}$$

The Cabot TBLE model (Cabot 1996) uses the eddy viscosity model

$$\nu_t = \kappa (z + z_0) u_*, \tag{2.7}$$

where u_* is determined using MOST and a reference level $z = z_{wl} \simeq 3.125$ m $\gg z_0$ above model bottom [see Wang et al. (2023) for further details].

2.3 ABL Spinup and Storm Initiation

The simulations' initial conditions are nearly identical to those used by Markowski (2020), with a westerly sheared, veering wind profile, and thermodynamic profiles similar to

those of Weisman and Klemp (1982; Fig. 2.2, 2.4). The WENO scheme is applied to scalar advection, but not to momentum advection. As in Markowski (2020), initial random 0.25-K temperature perturbations are implemented throughout the lowest 1 km such that the boundary layer can be considered turbulent. Prior to storm initiation, a 12-h spinup period allows a quasi-steady boundary layer to develop. Since each ensemble of storms utilizes a different near-surface turbulence model, each ensemble has its own corresponding spinup simulation from which its five members originate. By the end of the 12-h spinup period, each boundary layer's mean fields are very similar to each other, despite the variation in near-surface turbulence scheme (Fig. 2.2, 2.3, 2.4).

The environment is highly favorable for tornadoes, and its lack of a surface heat flux best represents a "late-day boundary layer" (Markowski 2020). Post-spinup, a warm, moist bubble (having a 4-K maximum potential temperature perturbation (θ'), 95% relative humidity, a 10-km horizontal radius and a 1.4-km vertical radius) is inserted into the domain to initiate convection. The location of warm bubble insertion varies with each ensemble member, but is consistent across the three ensembles (Table 2.4). Storms are triggered by the warm bubble and subsequently split, with the cyclonic supercells becoming dominant. The simulations continue for two hours post-warm-bubble-insertion.

2.4 Analysis Techniques

Although the simulations performed in this study are relatively high-resolution, the model grid spacing is insufficient to adequately resolve tornadoes. Thus, supercells in this study are considered tornadic when they produce TLVs. This study recognizes TLVs as vortices having a surface vertical vorticity (ζ_{sfc}) exceeding 0.5 s^{-1} and a ground-relative horizontal velocity exceeding 29 m s^{-1} at the lowest vertical grid level (z = 7.5 m). TLV magnitude is assigned using the "Enhanced Fujita Scale," or EF-scale.

As described by Markowski (2024), there are multiple methods traditionally used to identify surface-layer turbulent coherent structures; however, this study takes advantage of the coherent structures' associated longitudinal velocity and ζ streaks as a relatively simple means of identification.

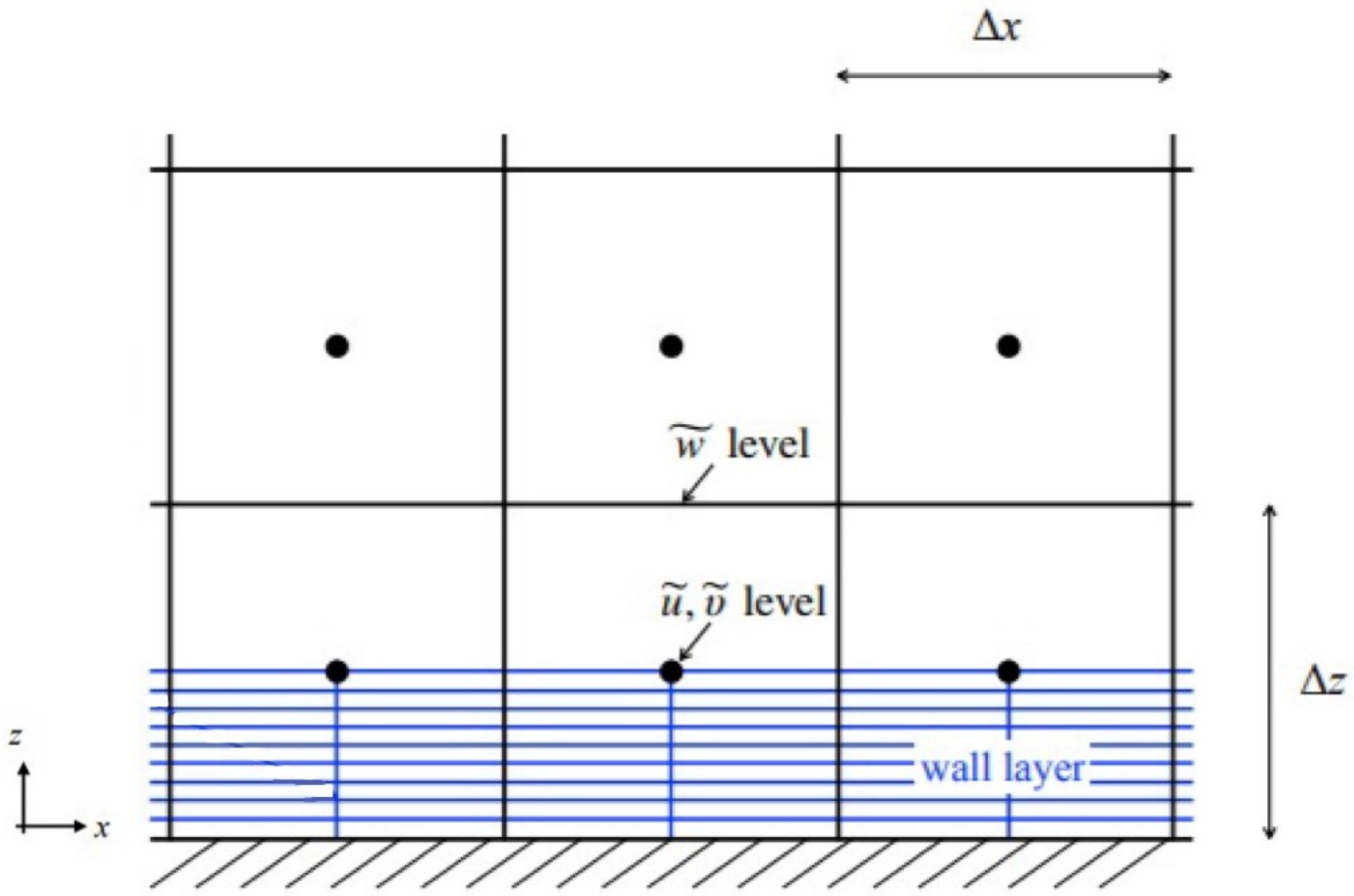

Figure 2.1. Illustration of the TBLE model's near-surface layer (i.e., wall layer) within the LES domain. Tildes represent spatial filtering over an LES grid cell, where δx and δz are the LES horizontal and vertical grid spacing, respectively. Adapted from Figure 1 in Wang et al. (2023).

	Storm(s) 1	Storm(s) 2	Storm(s) 3	Storm(s) 4	Storm(s) 5
x-location	0 km	0 km	2 km	2 km	0 km
y-location	2 km	0 km	0 km	2 km	-2 km
z-location	1.4 km	1.4 km	1.4 km	1.4 km	1.4 km

Table 2.1. Location of warm bubble insertion (at $t = 12$ h) for each ensemble's members.

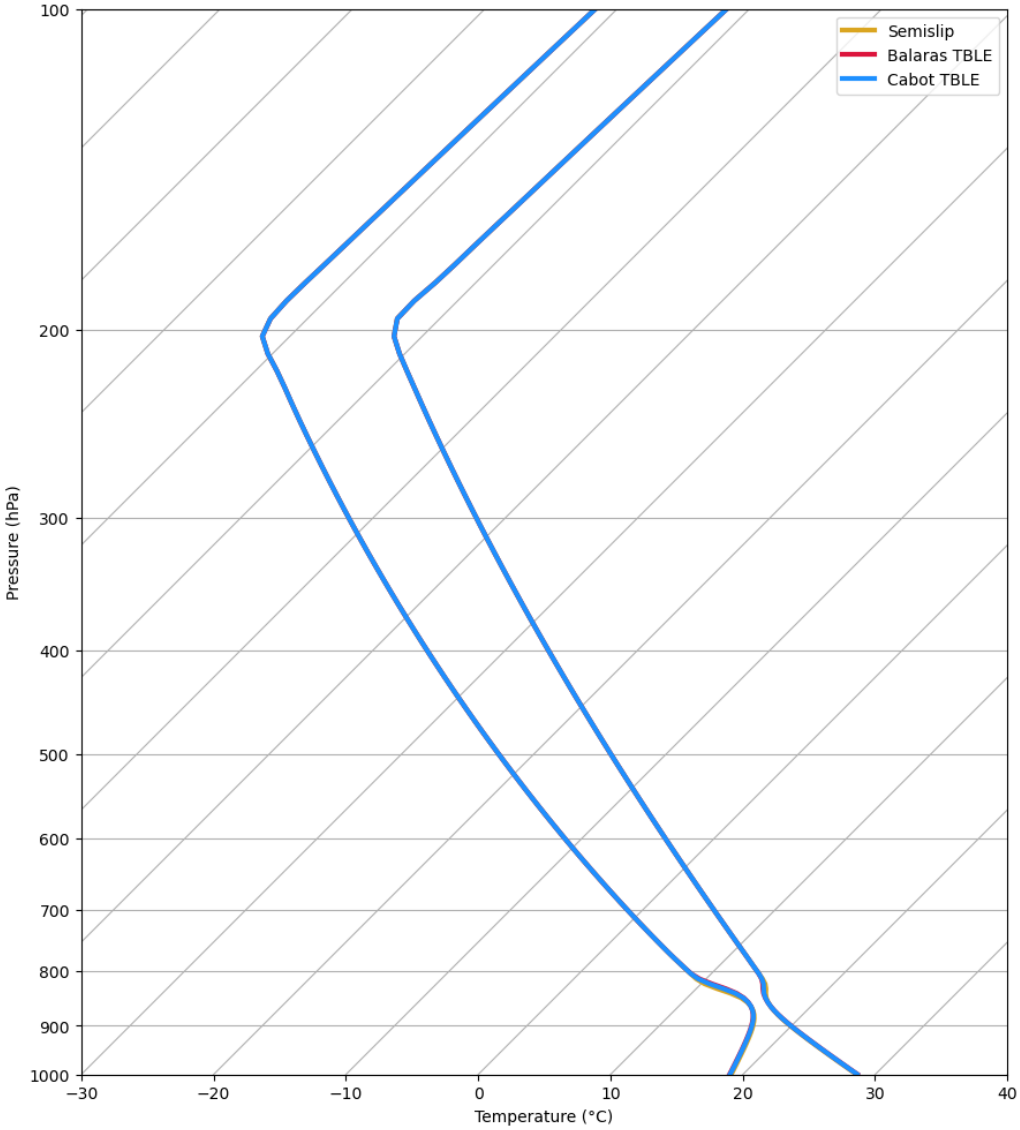

Figure 2.2. Statistically identical domain-averaged soundings at $t = 12$ h for each ensemble's spinup simulation.

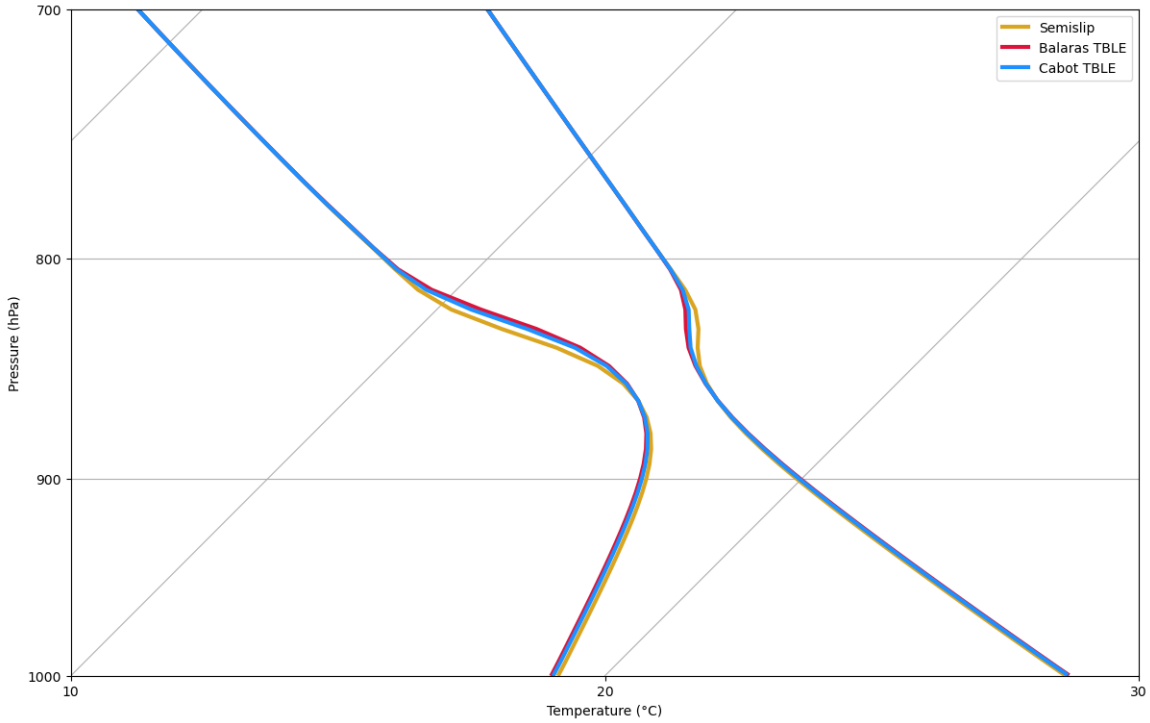

Figure 2.3. A close-up of the domain-averaged soundings at $t = 12$ h from Figure 2.2 reveals negligible differences in the spinup simulations' vertical temperature and dewpoint temperature profiles.

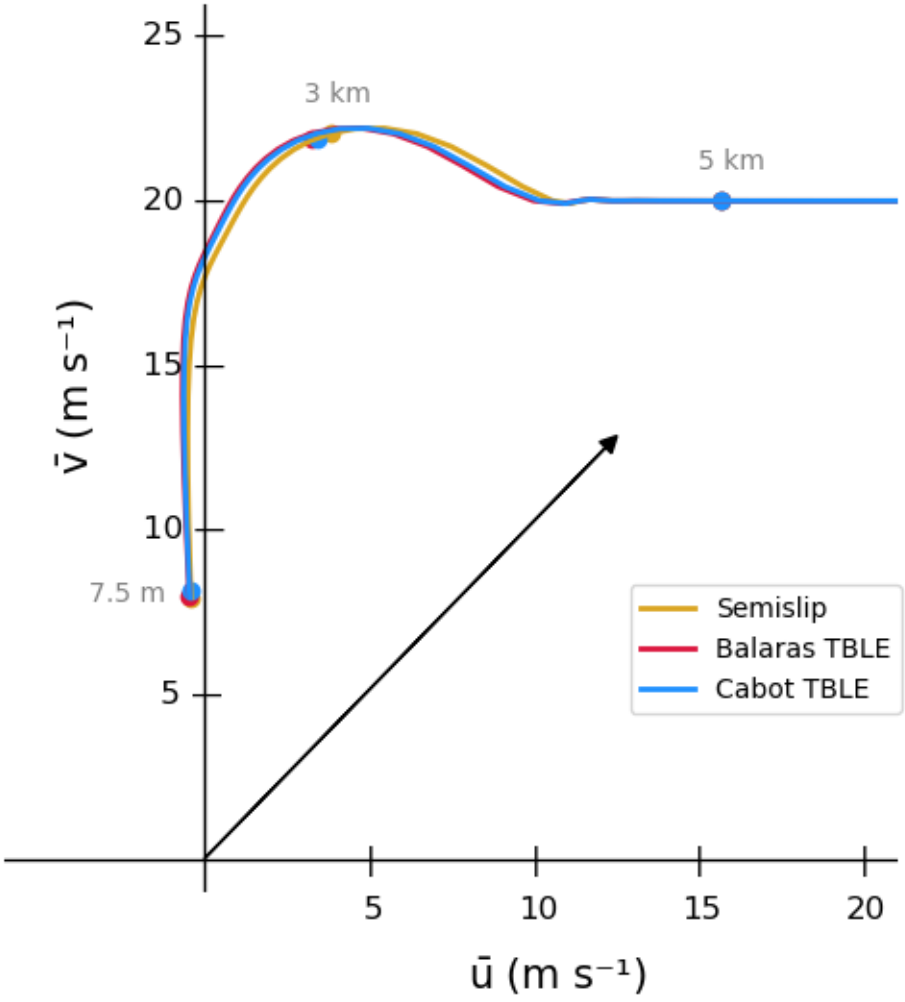

Figure 2.4. Domain-averaged hodographs (e.g., vertical wind profiles) at $t = 12$ h for each spinup simulation. The black arrow represents the right-mover's storm motion.

Chapter 3

Results

3.1 TBLE Influence on Pre-Storm Environment

At the end of the 12-h spinup period, each simulated ABL arrives at a quasi-steady state. For each boundary layer, the magnitude of the stress at the lower boundary was calculated following

$$\tau_w = \sqrt{\tau_{13}^2 + \tau_{23}^2} = u_*^2, \tag{3.1}$$

and is plotted against $\widetilde{U}_1$ at $t = 12$ h (Fig. 3.1). These so-called stress-strain-rate relationships reveal that each near-surface turbulence parameterization had the anticipated influence on its ABL: the semislip scheme's aforementioned assumption of a local, instantaneous balance between $\widetilde{U}_1$ and τ_w appears in the form of a nearly quadratic stress-strain-rate relationship. Conversely, the TBLE boundary layers demonstrate a significant departure from this clearly defined relationship.

Turbulent coherent structures can also be identified in each ensemble's pre-storm surface layer, via their associated longitudinal ζ streaks. Figure 3.2 displays these ζ streaks, and it can be seen that those in the TBLE surface layers are of higher magnitude (frequently

reaching $\sim$0.06 s^{-1}) than those in the semislip surface layer (occasionally reaching $\sim$0.04 s^{-1}). The TBLE also sees more numerous ζ streaks (there is less domain where $\zeta \approx 0$ in the TBLE simulations, yet the streaks remain similar in their relative width).

3.2 TBLE Influence on Near-Storm Environment

Each supercell simulation produces at least one TLV during the storm analysis period (t = 60–120 min). Storm output prior to t = 60 min is not discussed in this thesis, due to the unphysical nature of the warm bubble initiation method and its potential implications on early storm evolution (hereafter, t refers to the time elapsed since storm initiation, rather than spinup initiation). On average, the semislip ensemble's TLVs are the weakest, and the TBLE ensembles' TLVs are notably stronger (Fig. 3.3). The semislip ensemble's average TLV magnitude reaches EF-2 status, with a maximum $\widetilde{U}_1$ of 53.9 m s^{-1}. The Balaras TBLE and Cabot TBLE ensembles' average TLV magnitudes both achieve EF-3 status, with a maximum $\widetilde{U}_1$ of 69.0 m s^{-1} and of 68.4 m s^{-1}, respectively. TLV existence within each ensemble can be broken into four general periods; first, each ensemble's storms are non-tornadic from t = 60 min to $t \approx$ 80 min after initiation. Each ensemble's storms then develop very brief, sporadic TLVs beginning at $t \approx$ 80 min and lasting until $t \approx$ 95–100 min, depending on the ensemble. Subsequently, a period where none of the ensembles' storms generate a TLV occurs. This inactive period varies in length across the ensembles. The semislip ensemble's inactive period lasts from $t \approx$ 99–105 min ($\sim$6 min; Fig. 3.3a); the Balaras TBLE ensemble's inactive period occurs from $t \approx$ 97–98 min ($\sim$1 min; Fig. 3.3b); the Cabot TBLE ensemble's inactive period occurs at $t \approx$ 103 min ($<$1 min; Fig. 3.3c). Finally, for the remaining 15–20 min of simulation time, each ensemble's storms produce sustained TLVs.

Semislip storm number 1, Balaras TBLE storm number 5, and Cabot TBLE storm number 1 yield the most intense TLVs within each ensemble (reaching wind speeds corre-

sponding to low-end (78.4 m s^{-1}), high-end (87.9 m s^{-1}), and medium-strength (84.0 m s^{-1}) EF-4 tornadoes, respectively). Figure 3.4 displays each ensemble's strongest TLV and parent supercell over t = 90–120 min, at 10-minute intervals. The turbulent coherent structures that make up the simulations' surface layers are also apparent in Fig. 3.4, and they are, of course, interacting with the storms. The TBLE simulations' surface-layer ζ streaks are again stronger than the semislip's, and often reach near-TLV magnitudes even before crossing over to the cold side of the gust front boundary. The TBLE's higher ζ_{sfc} magnitudes are coupled with notably chaotic near-surface gust fronts and disorganized mid-level vertical velocity (w) fields. The semislip storm's gust front isopleth takes on a similar pattern as in the Markowski (2020) simulations, with the relatively smooth gust front adjacent to and beginning to wrap around the TLV. Conversely, the TBLE storms' near-surface gust fronts seem to be greatly affected by the non-equilibrium approach to modeling near-surface turbulence.

Figure 3.5 reveals the boundary layer stress-strain-rate relationships at t = 2 h, for the simulation producing the most intense TLV in each ensemble. While each boundary layer displays a wider range of both τ_w and $\widetilde{U}_1$ values than they did prior to storm initiation (Fig. 3.1), it can be seen that using the semislip scheme still results in that instantaneous, local equilibrium, as illustrated by the quadratic stress-strain-rate relationship. The TBLE simulations again do not demonstrate this clear relationship. Additionally, each simulation's near-storm environment exhibits a larger range of both τ_w and $\widetilde{U}_1$ values compared to the region of storm outflow (where there is non-negligible near-surface precipitation).

3.3 TBLE Influence on Storm Properties

Thunderstorms' overall magnitudes can be compared using the strength of their upward vertical motion. Within each simulation ensemble created in this study, the supercells are all similar in strength, as shown by time series of the domain-maximum w occurring over

each storm's lifetime (Fig. 3.6). Thus, choice of near-surface turbulence parameterization does not impact overall storm intensity, at least as defined by peak w.

Supercells' simulated reflectivity fields provide information about the storms' precipitation intensity, distribution, and low-level storm structure. Figure 3.7 depicts time series of each ensemble's average volume of "significant" reflectivity (determined via minimum thresholds of 45 and 50 dBZ, respectively). It can be gathered that, for the majority of the analysis period, the TBLE storms contain a larger volume of significant reflectivity compared to the semislip storms. Evidence of this result can be seen when comparing reflectivity fields from the storms that produce the strongest TLV in each ensemble. Figure 3.8 depicts much larger and stronger regions of intense reflectivity within the TBLE storms than in the semislip storm, especially as the storms evolve toward the end of the simulation time. Further, the TBLE storms' moderate precipitation extends far east of their gust front boundaries by $t =$ 120 min, while the semislip storm's moderate precipitation notably remains west of its gust front.

Figure 3.9 displays low-level $\boldsymbol{\omega}_h$ fields from the storms that produce the strongest TLV in each ensemble at $t =$ 90-120 min. The TBLE simulations' $\boldsymbol{\omega}_h$ fields are noticeably stronger and indicate more turbulence, especially in the storms' inflow regions. This result was expected, given the TBLE surface layers' stronger turbulent coherent structures. Each of the storms also have more laminar, near-zero $\boldsymbol{\omega}_h$ in their cores.

Cold pools, or regions of relatively cold, dense air in thunderstorms, result from evaporative cooling and greatly influence supercell dynamics. Figure 3.10 provides time series of each storm ensemble's average cold pool volume and average low-level cold pool area, respectively. Here, a storm's cold pool volume is calculated as the domain volume from $z = 22.5$–522 m where $\theta' < -2$ K, and a cold pool's low-level area is calculated as the domain area where $\theta' < -2$ K at the model's lowest grid level ($z = 7.5$ m). At each time step, θ' is

calculated as $\theta' = \theta - \overline{\theta}_{\text{env}}$, where $\overline{\theta}_{\text{env}}$ represents the average environmental base state far away from convection. The Cabot TBLE ensemble exhibits a larger average volume and a larger average area of cold outflow than the Balaras TBLE and semislip ensembles do, for the last ∼20 min of the simulations. This result is likely not due to differences in condensate mass, given the reflectivity time series shown in Fig. 3.7.

Interestingly, the cold pools within the supercells that produced the strongest TLVs in each ensemble appear very different from each other (Fig. 3.11). By $t = 90$ min, the semislip storm's cold pool appears to be much more intense than the other ensembles' storms; however, by $t = 120$ min, the semislip storm's cold pool has significantly weakened, while the Cabot TBLE storm's cold pool has markedly strengthened.

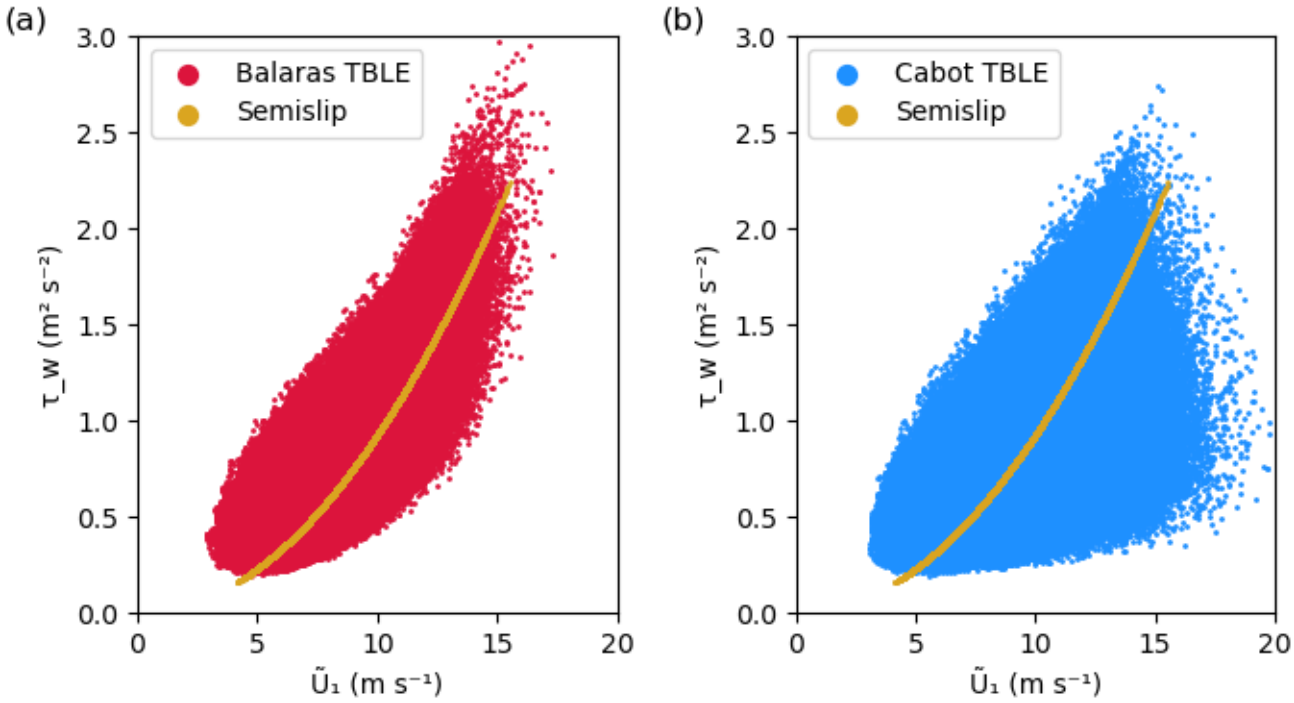

Figure 3.1. Instantaneous local $\widetilde{U}_1$ (m s^{-1}) at $z = 7.5$ m versus τ_w (m^2 s^{-2}) at $t = 12$ h for each spinup simulation. Gold (a-b), red (a), and blue (b) scatters represent results from the semislip, Balaras TBLE, Cabot TBLE simulations, respectively.

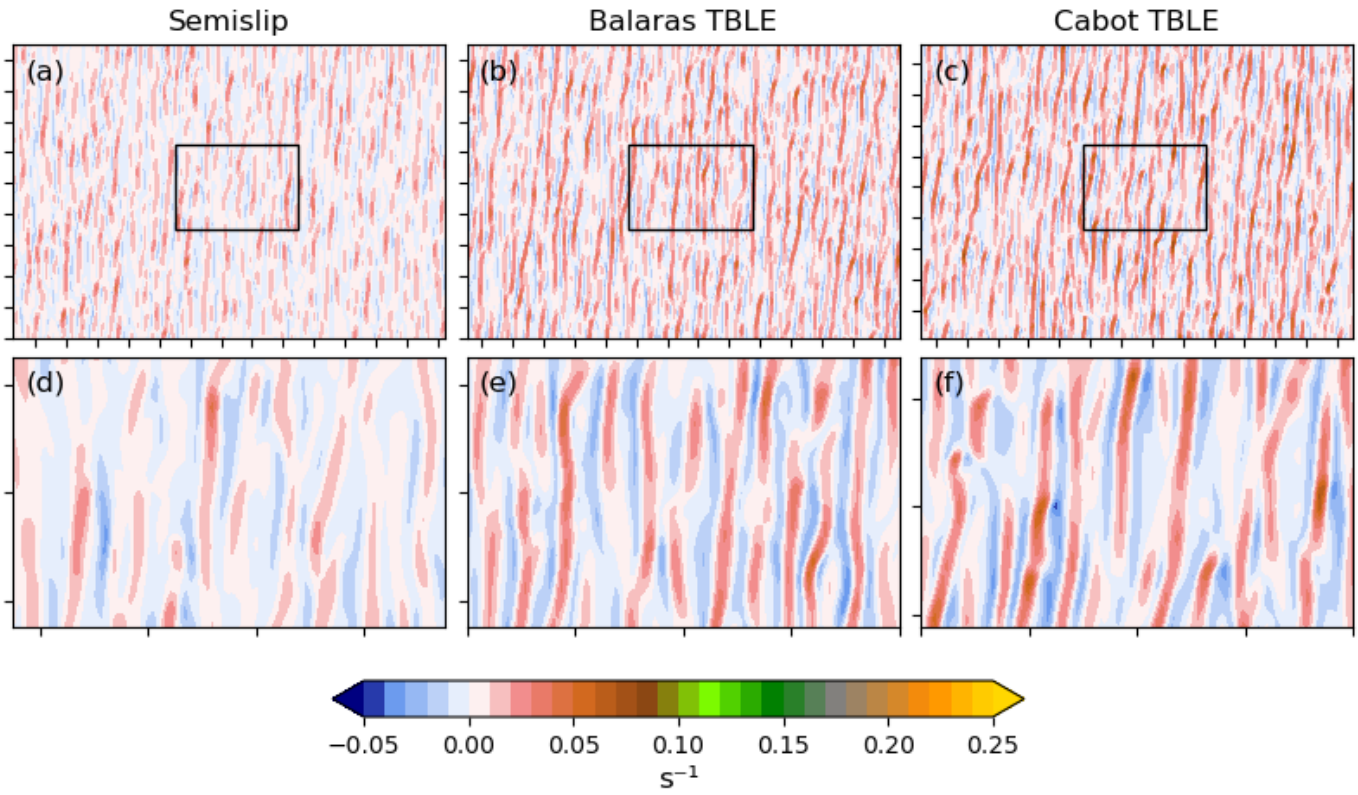

Figure 3.2. (a)–(c) Horizontal cross-sections (28 × 19 km) of ζ (s^{-1}) at $z = 7.5$ m (shaded) at $t = 12$ h in the (a) semislip ABL, (b) Balaras TBLE ABL, and (c) Cabot TBLE ABL. (d)–(f) Zoomed-in (8 × 5.5 km) versions of (a)–(c). The black boxes (a-c) represent the zoomed-in plots (d-f). Axis ticks are every 2 km.

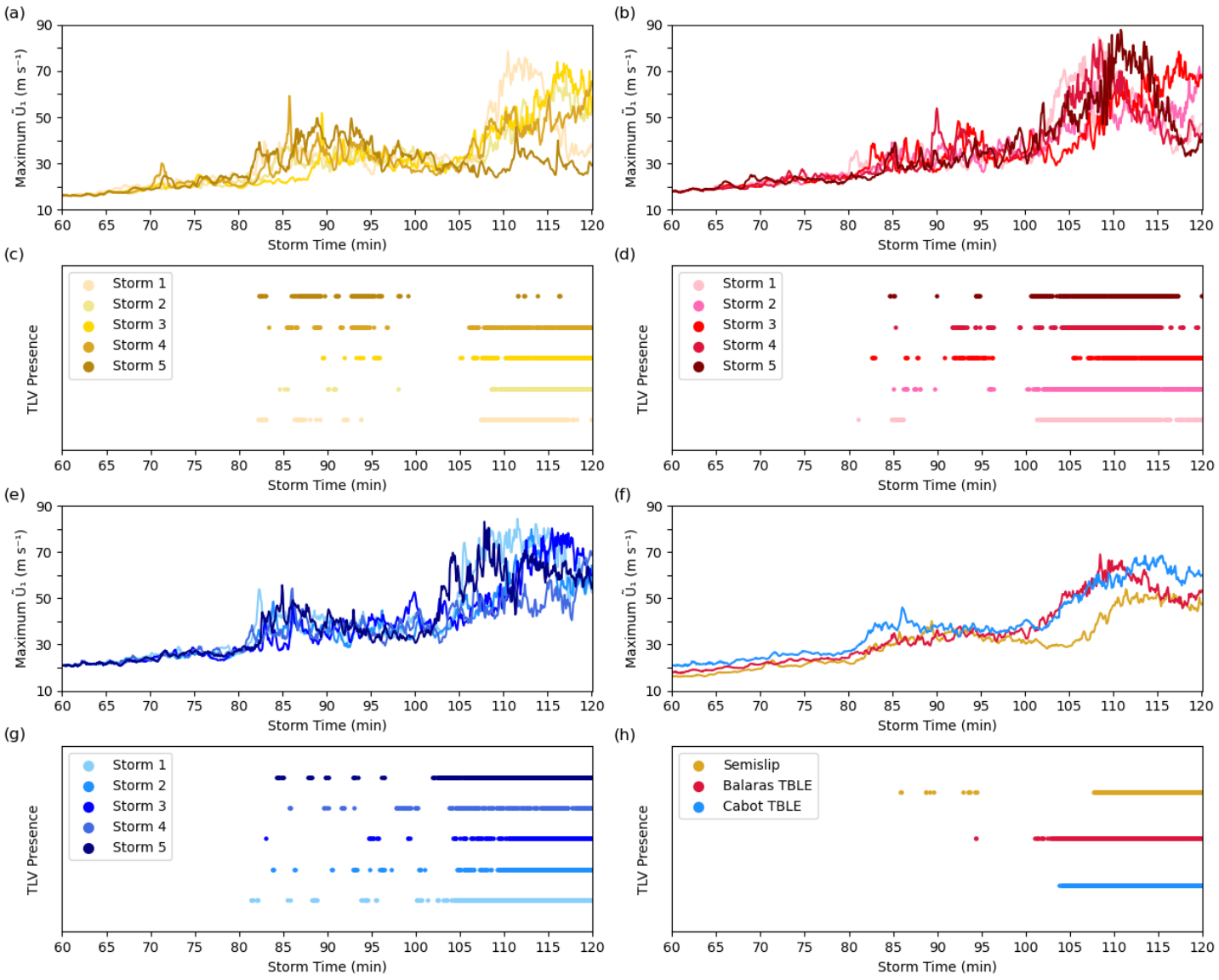

Figure 3.3. Maximum ground-relative horizontal wind speed (m s^{-1}; line plots) at the lowest model level over $t = 60$–120 min in the (a) semislip ensemble members, (b) Balaras TBLE ensemble members, (e) Cabot TBLE ensemble members, as well as for (f) each ensemble average. Times at which there is a TLV present (dotted plots) in the (c) semislip ensemble members, (d) Balaras TBLE ensemble members, (g) Cabot TBLE ensemble members, as well as for (h) each ensemble average, over $t = 60$–120 min.

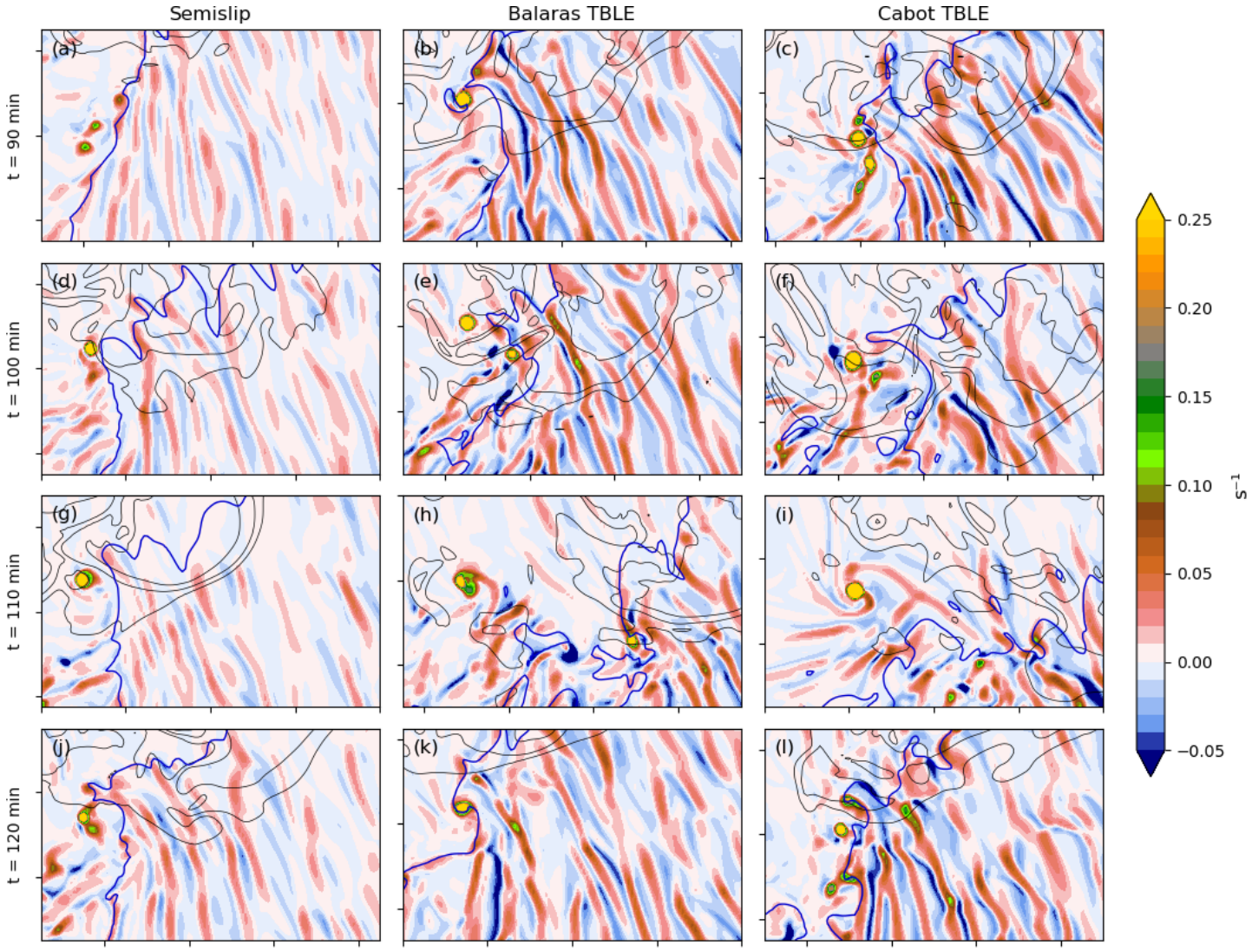

Figure 3.4. Horizontal cross-sections of ζ (s^{-1}) at $z = 7.5$ m (shaded) and w at $z = 522$ m (black isotachs of 15, 25, 35 m s^{-1}) at $t = 90$, 100, 110, and 120 min for semislip storm 1 (a,d,g,j), Balaras TBLE storm 5 (b,e,h,k), and Cabot TBLE storm 1 (c,f,i,l). The $\theta' = -0.25$ K isopleth (bold blue contour) indicates the gust front position. Axis ticks are every 2 km.

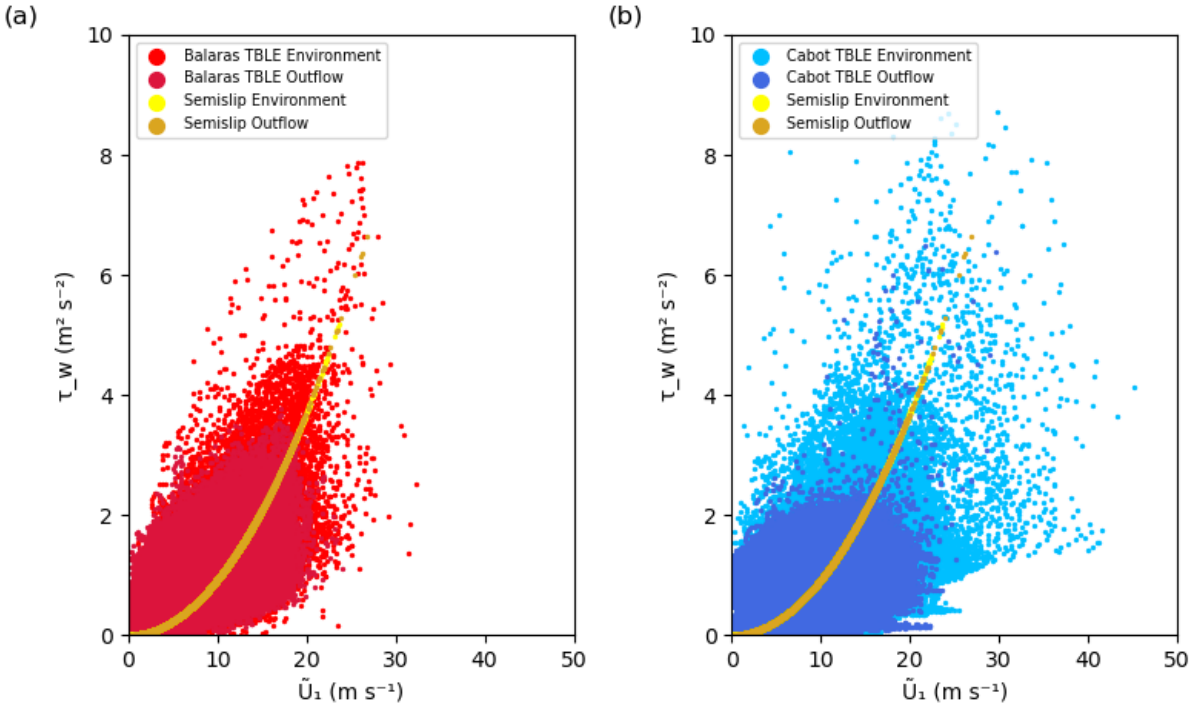

Figure 3.5. Instantaneous, local $\widetilde{U}_1$ (m s^{-1}) at $z = 7.5$ m versus τ_w (m^2 s^{-2}) at $t = 120$ min for the storm environments with the strongest TLVs. Yellow (a-b), light red (a), and light blue (b) scatters represent results from the semislip, Balaras TBLE, and Cabot TBLE environments, respectively. Gold (a-b), dark red (a), and dark blue (b) scatters represent results from the semislip, Balaras TBLE, and Cabot TBLE storm outflow, respectively. The region of the domain where near-surface ($z = 7.5$ m) reflectivity ≥ 10 dBZ is considered to be storm outflow; the rest of the domain is considered to be near-storm environment.

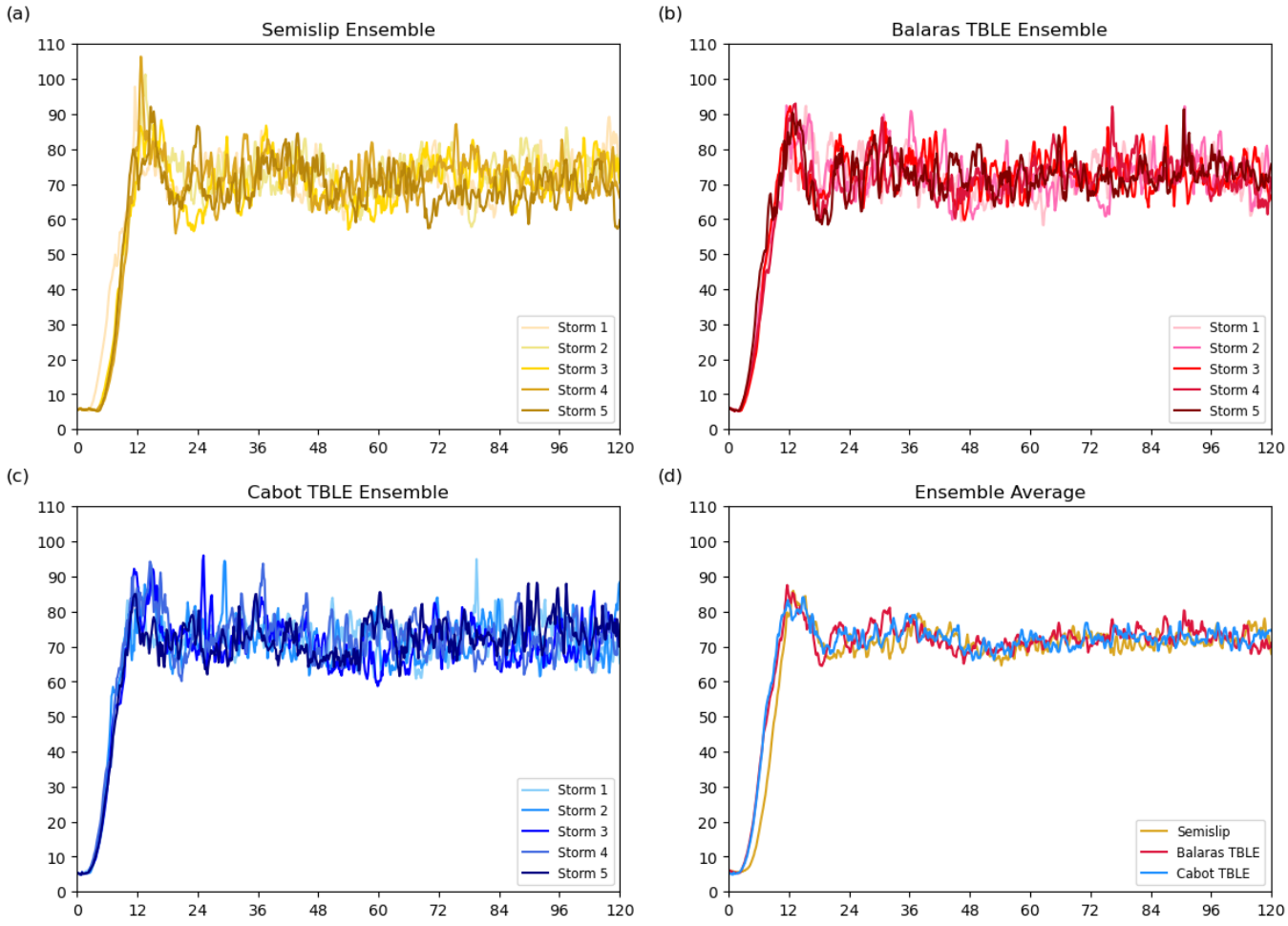

Figure 3.6. Domain-maximum w (m s^{-1}) time series for all five storms in the (a) semislip, (b) Balaras TBLE, and (c) Cabot TBLE storm ensembles, as well as (d) the ensemble means.

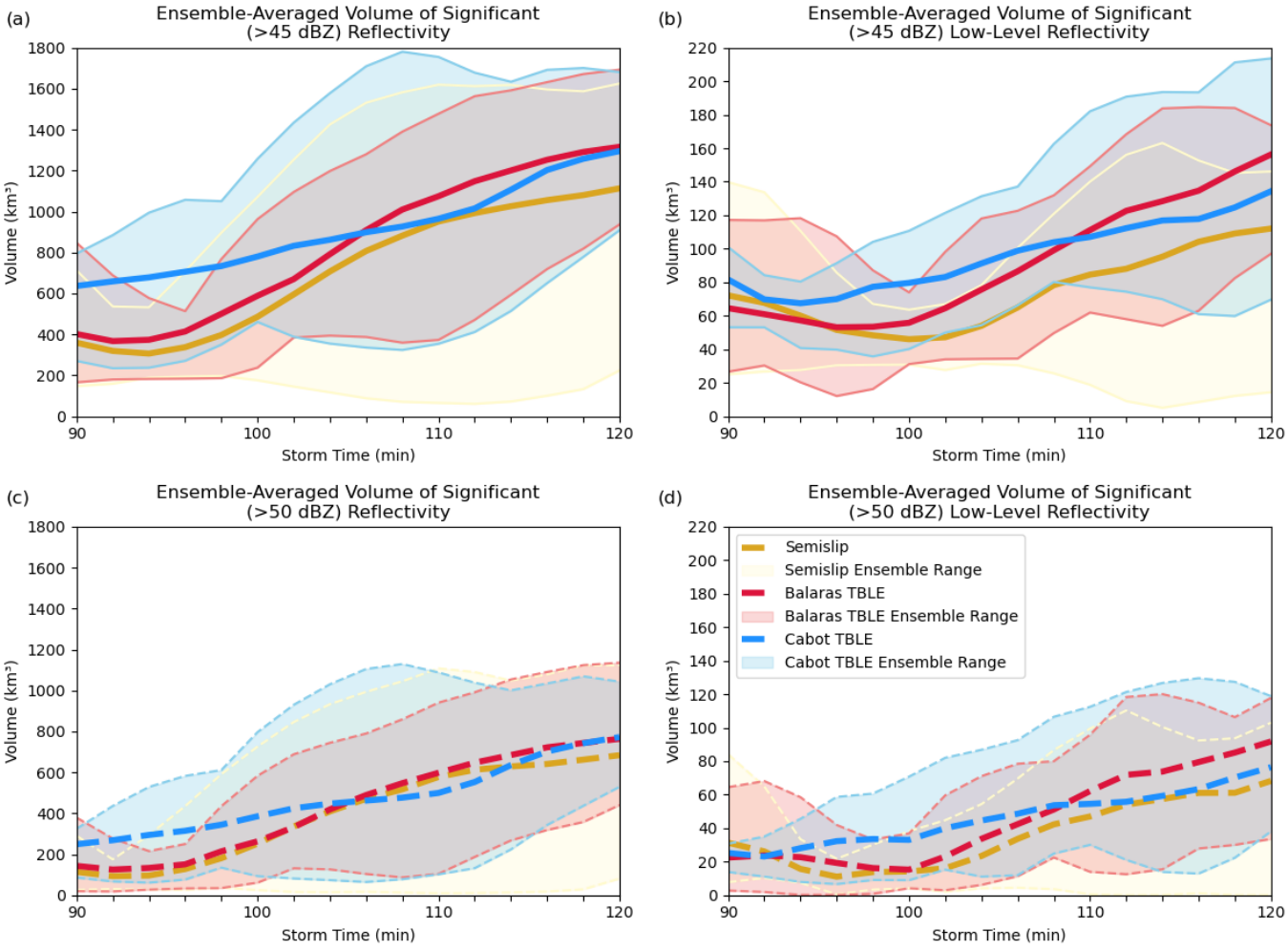

Figure 3.7. Ensemble-averaged time series of (a) the domain volume where reflectivity >45 dBZ over t = 90–120 min, (b) the $z \leq 1$ km volume where reflectivity >45 dBZ over t = 90–120 min, (c) the domain volume where reflectivity >50 dBZ over t = 90–120 min, and (d) the $z \leq 1$ km volume where reflectivity >50 dBZ over t = 90–120 min.

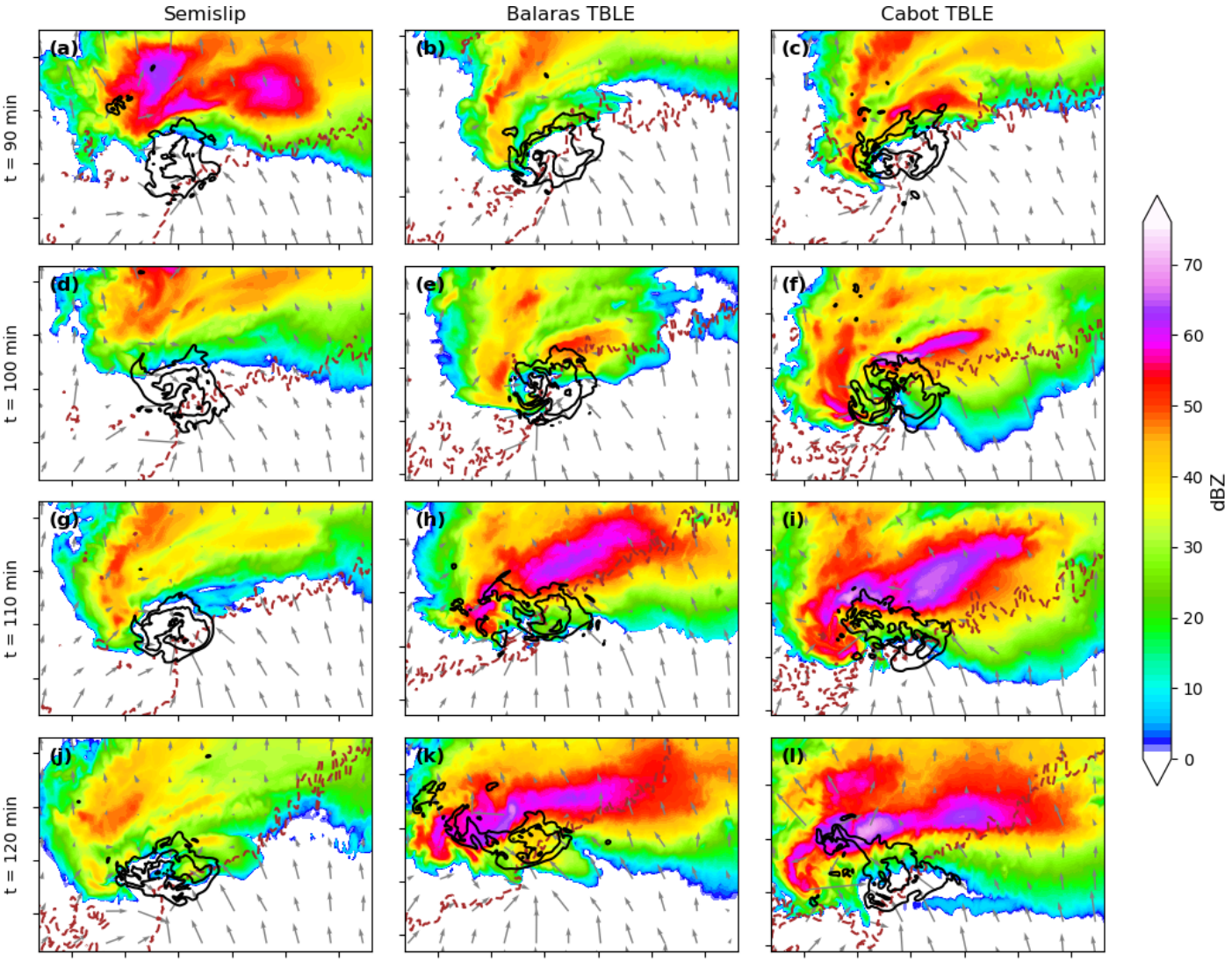

Figure 3.8. Reflectivity (dBZ) at $z = 522$ m (shaded), w at $z = 5$ km (black isotachs at 15, 30, and 45 m s^{-1}), $\widetilde{U}_1$ (gray barbs; m s^{-1}), and gust front position (brown dashed line; $\theta' = -0.25$ K at the lowest grid level) at $t = 90$–120 min for the storm that produces the strongest TLV in each ensemble. Axis ticks are every 5 km.

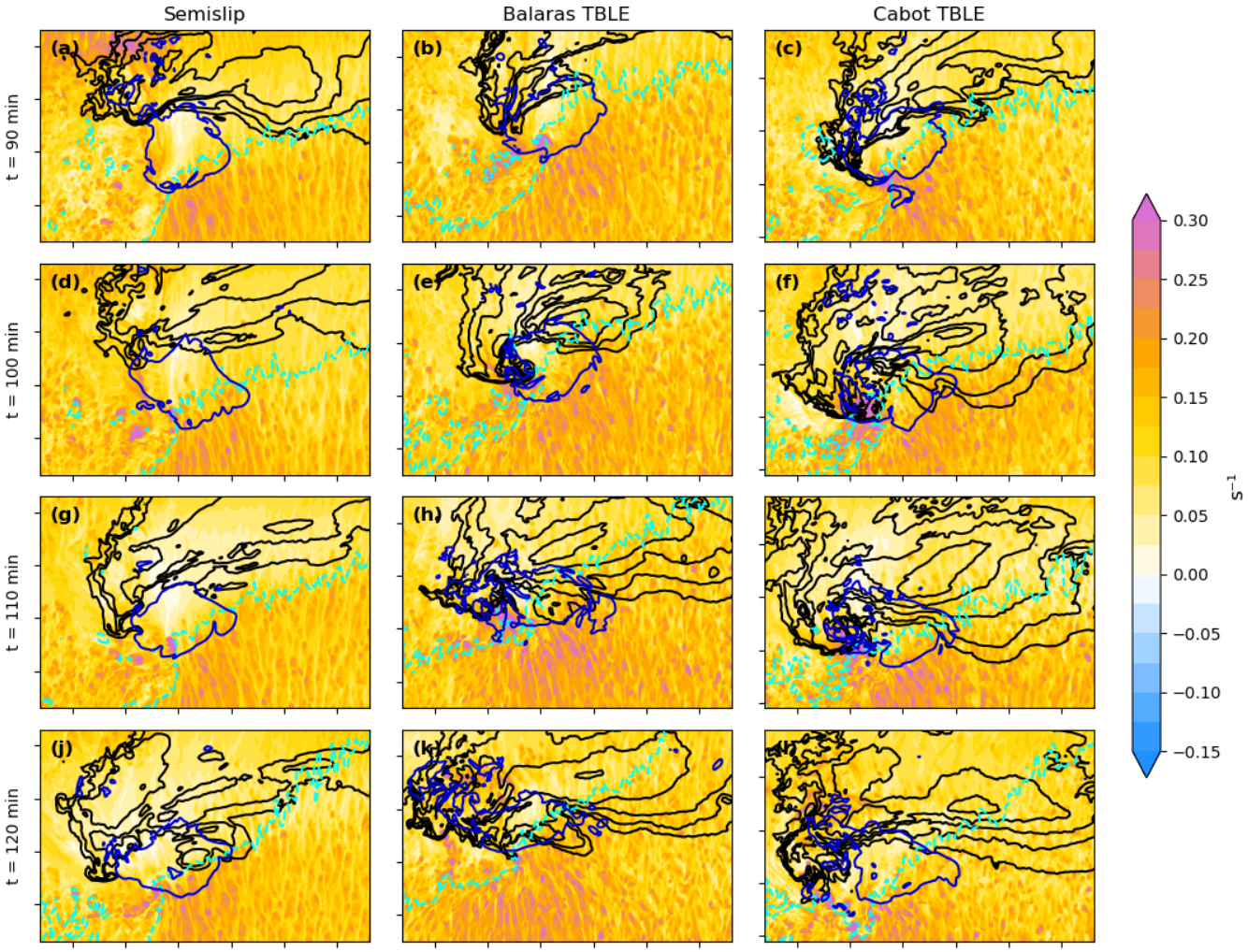

Figure 3.9. Horizontal $\boldsymbol{\omega}_h$ (s^{-1}) cross-sections at $z = 22.5$ m (shaded) at $t = 90$–120 min for the storm that produces the strongest TLV in each ensemble. The $w = 10$ m s^{-1} isotach at $z = 5$ km (dark blue contour) and reflectivity at $z = 522$ m (black contours of 20, 30, 40, 50, and 60 dBZ) are overlaid. The $\theta' = -0.25$ K isopleth (dashed cyan contour) indicates near-surface ($z = 7.5$ m) gust front position. Axis ticks are every 5 km.

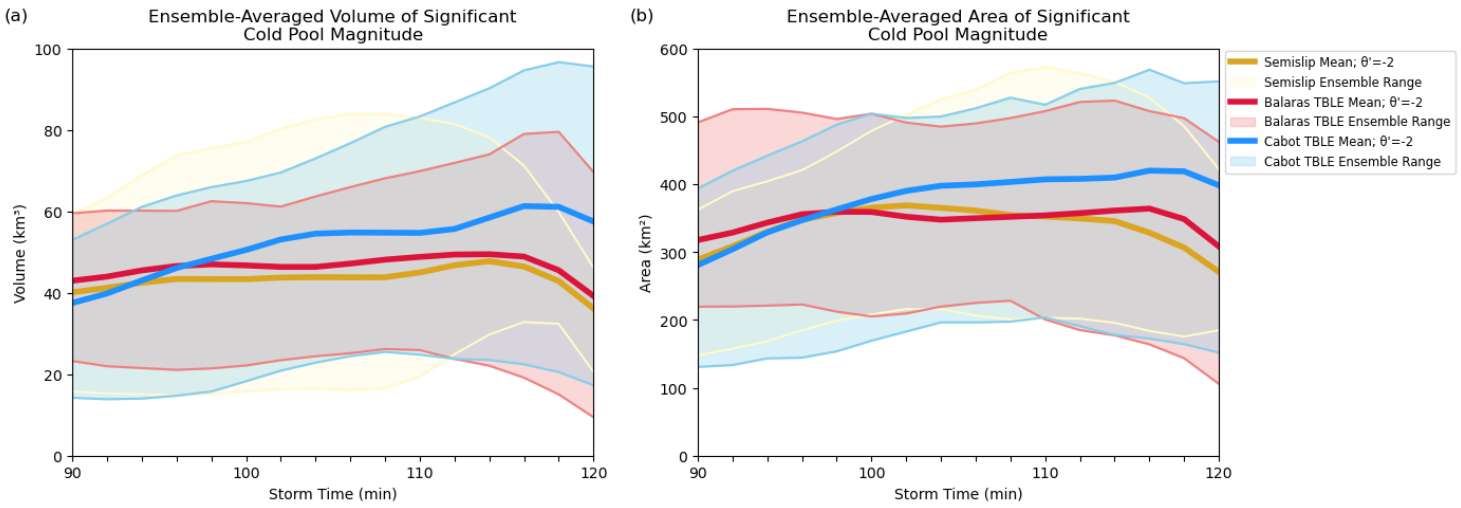

Figure 3.10. Ensemble-averaged time series of (a) the $z \leq 500$ m domain volume where $\theta' < -2$ K over $t = 90$–120 min, and (b) the domain area where $\theta' < -2$ K at the lowest grid level ($z = 7.5$ m) over $t = 90$–120 min. Bold lines represent ensemble averages, and each ensemble's minimum and maximum values are indicated by corresponding pastel lines, with shaded ranges.

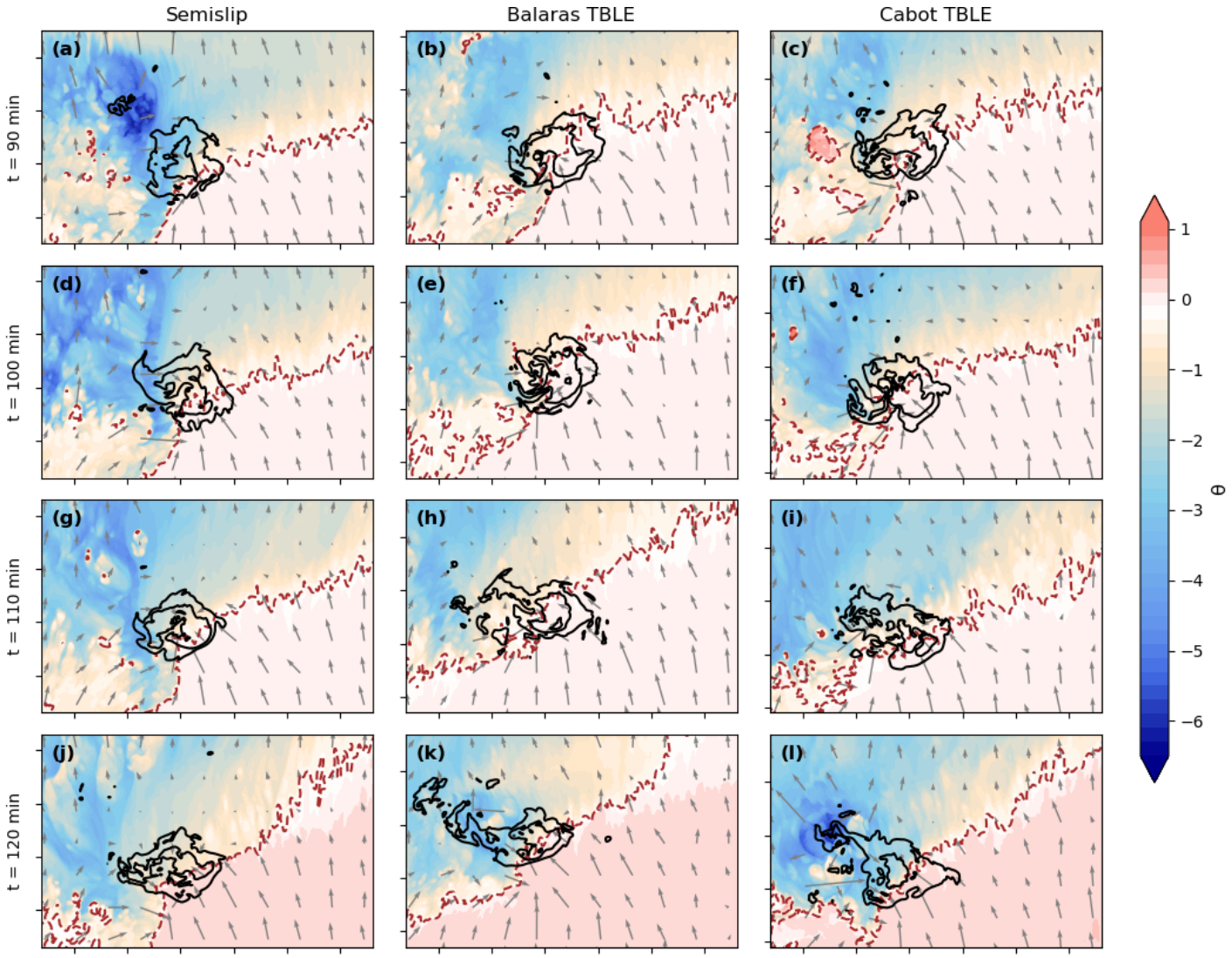

Figure 3.11. Horizontal θ' (K) cross-sections at $z = 7.5$ m (shaded) at $t = 90$–120 min for the storm that produces the strongest TLV in each ensemble. Black isotachs denote w at $z = 5$ km (15, 30, and 45 m s^{-1}), $\widetilde{U}_1$ (gray barbs; m s^{-1}), and gust front position (brown dashed line; $\theta' = -0.25$ K at the lowest grid level) are overlayed. Axis ticks are every 5 km.

Chapter 4

Conclusions

In this study, three five-member ensembles of tornadic supercell storms were simulated in turbulent environments that each used a different near-surface turbulence parameterization method: the semislip scheme, the Balaras TBLE approach, or the Cabot TBLE approach. The pre-storm boundary layers and the storms' initial conditions were identical to those of Markowski (2020), with the exception that the WENO scheme is applied only to the advection of scalars in this study (as opposed to both scalar and momentum advection). The WENO scheme for scalar advection is critical in order to avoid spurious oscillations near sharp scalar gradients (Shu 2003), but applying the WENO scheme to momentum advection can lead to unrealistic suppression of turbulent motions in LES (Wang et al. 2021). Due to this WENO configuration adjustment, differences in this work's semislip storm ensemble and the Markowski (2020) simulations can be attributed to the choice of WENO advection scheme. Strong, long-lived supercell storms occurred in all fifteen simulations, and each produced at least one strong TLV. As storms within each ensemble only differed in the location of warm-bubble initiation, any variation within a storm ensemble can be attributed to the initial warm bubble's interaction with turbulent boundary layer structures (Markowski 2020).

The results of this work suggest that choice of near-surface turbulence parameterization plays a role in the occurrence and magnitude of surface-layer turbulent coherent structures. Given Markowski's (2024) "new pathway for tornadogenesis," these results suggest that the TBLE approach to parameterizing near-surface turbulence might make tornadogenesis more likely to occur than the semislip scheme does.

Results also indicate that the near-surface turbulence parameterization has a significant impact on TLV magnitude and duration. Each simulation produces at least one TLV, but both TBLE ensembles' mean TLV magnitudes achieve EF-3 status, while the semislip ensemble's mean TLV only reaches EF-2 strength. Additionally, results suggest that choice of near-surface turbulence parameterization appreciably affects supercells' reflectivity fields. The TBLE ensembles' average volumes of significant reflectivity exceed the semislip ensemble's average significant reflectivity volume for the vast majority of the analysis period, regardless of the threshold used to determine significance. The ensembles' significant cold pools were less variable on average, although the Cabot TBLE ensemble harbored the most cold outflow for the last $\sim$20 min of simulation time. Near-surface $\boldsymbol{\omega}_h$ fields were relatively consistent across each ensemble, with the exception of the TBLE ensembles' $\boldsymbol{\omega}_h$ indicating more turbulence. Finally, near-surface turbulence parameterization does not affect overall storm strength.

Though it is difficult to verify whether the TBLE approach to the parameterization of near-surface turbulence is "better" than the semislip scheme, the TBLE approach at least uses one less incorrect assumption. Removing such implicit assumptions from our parameterization of near-surface turbulence can only lead to a more justified representation of storm dynamics in simulations, and is crucial to furthering our current understanding of supercell storms and tornadogenesis.

Bibliography

Alfonsi, G., 2006: Coherent structures of turbulence: Methods of education and results. *Applied Mechanics Reviews*, **59 (6)**, 307–323, doi:10.1115/1.2345370.

Balaras, E., C. Benocci, and U. Piomelli, 1996: Two-layer approximate boundary conditions for large-eddy simulations. *Amer. Inst. Aeronaut. Astronaut.*, **34 (6)**, 123–135, doi:10.2514/3.13200.

Bryan, G. H. and J. M. Fritsch, 2002: A benchmark simulation for moist nonhydrostatic numerical models. *Mon. Wea. Rev.*, **130 (12)**, 2917–2928, doi:10.1175/1520-0493(2002)130<2917:ABSFMN>2.0.CO;2.

Cabot, W., 1996: Near-wall models in large eddy simulations of flow behind a backward-facing step. *Annual Research Briefs*, 199–210.

Davidson, P. A., 2015: *Turbulence: An Introduction for Scientists and Engineers*. Oxford University Press, 630 pp.

Davies-Jones, R. P., 1982a: A new look at the vorticity equation with application to tornadogenesis. Preprints, *12th Conf. on Severe Local Storms*, San Antonio, TX, Amer. Meteor. Soc., 249-252.

Davies-Jones, R. P., 1982b: Observational and theoretical aspects of tornadogenesis. *Intense Atmospheric Vortices*, L. Bengtsson and J. Lighthill, Eds., Springer-Verlag, 175–189.

Davies-Jones, R. P., 1984: Streamwise vorticity: The origin of updraft rotation in supercell storms. *J. Atmos. Sci.*, **41 (20)**, 2991–3006, doi:10.1175/1520-0469(1984)041<2991:SVTOOU>2.0.CO;2.

Davies-Jones, R. P. and H. E. Brooks, 1993: Mesocyclogenesis from a theoretical perspective. *The Tornado: Its Structure, Dynamics, Prediction, and Hazards*, Geophys. Monogr., No. 79, Amer. Geophys. Union, 105–114.

Deardorff, J. W., 1980: Stratocumulus-capped mixed layer derived from a three-dimensional model. *Bound.-Layer Meteor.*, **18**, 495–527, doi:10.1007/BF00119502.

Klemp, J. B. and R. B. Wilhelmson, 1978: The simulation of three-dimensional convective storm dynamics. *J. Atmos. Sci.*, **35 (6)**, 1070–1096, doi:10.1175/1520-0469(1978)035<1070:TSOTDC>2.0.CO;2.

Markowski, P. and Y. Richardson, 2010: *Mesoscale meteorology in midlatitudes*. John Wiley & Sons, Ltd, doi:10.1002/9780470682104.

Markowski, P. M., 2020: What is the intrinsic predictability of tornadic supercell thunderstorms? *Mon. Wea. Rev.*, **148 (8)**, 3157–3180, doi:10.1175/MWR-D-20-0076.1.

Markowski, P. M., 2024: A new pathway for tornadogenesis exposed by numerical simulations of supercells in turbulent environments. *J. Atmos. Sci.*, **81 (3)**, 481–518, doi:10.1175/JAS-D-23-0161.1.

Moeng, C.-H. and P. P. Sullivan, 1994: A comparison of shear- and buoyancy-driven planetary boundary layer flows. *J. Atmos. Sci.*, **51 (7)**, 999–1022, doi:10.1175/1520-0469(1994)051<0999:ACOSAB>2.0.CO;2.

Monin, A. and A. Obukhov, 1954: Basic laws of turbulent mixing in the atmosphere near the ground. *J. Fluid Mech.*, **242**, 51–78, doi:10.1017/S0022112092002271.

Nowotarski, C. J., P. M. Markowski, Y. P. Richardson, and G. H. Bryan, 2014: Properties of a simulated convective boundary layer in an idealized supercell thunderstorm environment. *Mon. Wea. Rev.*, **142 (11)**, 3955–3976, doi:10.1175/MWR-D-13-00349.1.

Rotunno, R., 1981: On the evolution of thunderstorm rotation. *Mon. Wea. Rev.*, **109 (3)**, 577–586, doi:10.1175/1520-0493(1981)109<0577:OTEOTR>2.0.CO;2.

Rotunno, R. and J. Klemp, 1982: The influence of the shear-induced pressure gradient on thunderstorm motion. *Mon. Wea. Rev.*, **110 (2)**, 136–151, doi:10.1175/1520-0493(1982)110<0136:TIOTSI>2.0.CO;2.

Rotunno, R. and J. Klemp, 1985: On the rotation and propagation of simulated supercell thunderstorms. *J. Atmos. Sci.*, **42 (3)**, 271–292, doi:10.1175/1520-0469(1985)042<0271:OTRAPO>2.0.CO;2.

Shu, C.-W., 2003: High-order finite difference and finite volume weno schemes and discontinuous galerkin methods for cfd. *Int. J. Comput. Fluid Dyn.*, **17**, 107–118, doi:10.1080/1061856031000104851.

Wang, A., Y. Pan, G. H. Bryan, and P. M. Markowski, 2023: Modeling near-surface turbulence in large-eddy simulations of a tornado: An application of thin boundary layer equations. *Mon. Wea. Rev.*, **115 (6)**, 1587–1607, doi:10.1175/MWR-D-22-0060.1.

Wang, A., Y. Pan, and P. M. Markowski, 2021: The influence of weno schemes on large-eddy simulations of a neutral atmospheric boundary layer. *J. Atmos. Sci.*, **78**, 3613–3628, doi:10.1175/JAS-D-21-0033.1.

Weisman, M. L. and J. B. Klemp, 1982: The dependence of numerically simulated convective storms on vertical wind shear and buoyancy. *Mon. Wea. Rev.*, **110 (6)**, 504–520, doi: 10.1175/1520-0493(1982)110<0504:TDONSC>2.0.CO;2.

Wicker, L. J. and R. B. Wilhelmson, 1995: Simulation and analysis of tornado development and decay within a three-dimensional supercell thunderstorm. *J. Atmos. Sci.*, **52 (15)**, 2675–2703, doi:10.1175/1520-0469(1995)052<2675:SAAOTD>2.0.CO;2.